INT. J. NUM. METH. HEAT FLUID FLOW, VOL. 3, 531–544 (1993)

HIGH RESOLUTION NUMERICAL METHOD FOR PREDICTING SLOTS FILM-COOLING USING THE COUPLED PARABOLIC/ELLIPTIC NAVIER–STOKES SOLVER

E. Y.-K. NG

School of Mechanical & Production Engineering, Nanyang Technological University, Nanyang Avenue, Singapore 2263, Republic of Singapore

ABSTRACT

The suitability of a coupled scheme based on parabolic/elliptic Navier–Stokes equations for calculating film cooling flows and heat transfer downstream of flush, angled injection slots is explored. The coupled algorithm that combined the coarse mesh 'outer' Navier–Stokes and fine grid 'inner' parabolic Navier–Stokes codes makes retention of the current high resolution model desirable because an acceptable accuracy and economy of computation time are attainable using only mini-computer resources. The 'inner-code' includes the FLARE approximation to permit small reverse flow. The inner and outer codes are coupled by adopting an approach analogous to classical multigrid methods. It is found that for high blowing mass flow rate of 1.0 with the case of greater than 40° injection angle, the fully parabolic procedure is unable to cope with an extensive separation region immediately downstream of the slot; the present coupling methodology is crucial. The study involves the calculation of heat transfer rates on the surface downstream of the angled slot. Predicted film cooling effectiveness distribution together with the effects of governing parameters are described and show close agreement with the experimental data.

KEY WORDS Film cooling Navier–Stokes solver

NOMENCLATURE

h	average heat transfer coefficient,	ξ, η	transformed coordinates,
k	thermal conductivity,	ρ	fluid density,
u, v	velocity components in a Cartesian system,	δ	boundary layer thickness,
		Y_{max}	value of y at which $F(y)^1$ is maximum
$\hat{u}, \hat{v}$	contravariant velocity components,	G^*	mass velocity ratio,
U	vector of flow property,	Θ^*	a temperature difference ratio,
x, y	Cartesian coordinates,	$\varnothing$	a cooling effect parameter.

INTRODUCTION

Wall jets and film cooling are used in a wide range of engineering situations and have been extensively investigated in the past few years[6,7]. An example of the use of film cooling arises in gas turbines where the on-going quest for increased turbine inlet temperatures has generated the need for blade materials with better heat-resistance characteristics and/or better methods

0961–5539/93/060531–14$2.00

Received November 1992
Revised April 1993

of cooling the blades. One such method, which is attracting attention, is slot-film cooling (discrete-hole cooling for the 3-D case) in which low-temperature secondary fluid is supplied via passages within the blade to a slot leading to the surface, thereby forming a protective coolant film. However, the extent of the region that is protected by any one coolant source is limited, because of penetration by and mixing with the hot main stream. Such systems must, therefore, be designed with care. The accuracy of the predictions depends mainly on the correct calculation of the flow in the immediate vicinity of the slots where flow separation is highly probable with the implication that the proper equations describing the flow are elliptic, rather than parabolic. In this region, the injection of the secondary fluid is expected to significantly alter the flow pattern from that of the primary fluid alone, and the effective heat transfer coefficient may be either increased or decreased, depending on the amount and nature of the injection. Fully elliptic N–S codes can be used to predict viscous flows in general but can have large computer storage and CPU requirements. Such resource costs may discourage use for high resolution work. In particular, when resolution comparable to that used with conventional boundary layer methods is required (for heat transfer work, say), full N–S solvers become very expensive. The objective of this paper is to develop a methodology for performing high resolution 2-D Navier–Stokes computations but without consuming huge computer resources and it aims to improve the accuracy (and richness) of the slots film-cooling flow predictions.

In conventional viscous–inviscid coupling methods the viscous and inviscid regions are separated from one another and coupling is through information transfer near the interface ('zonal' approach), in the present work, both N–S and PNS codes are solved on a mesh covering the whole flow field. The N–S code provides an initial guess of global pressure field, runs on a coarse mesh and is referred to as the 'outer code'; the PNS solver runs on a much finer sub-mesh again covering the whole flow domain and is called the 'inner code'. The outer coarse grid code selected is the 2-D fully N–S code of Dawes[3] (equally an Euler solver would do). For the inner code, a parabolized 2-D N–S code was written by the author. Parabolized codes are basically boundary layer codes with the same advantages (speed, limited memory requirement) and limitations (in ability to handle reverse flow). The two codes are then coupled with the pressure field from the outer code driving the inner one and source terms derived from the inner solution in an analogous way to classical multigrid coupling sent back to the outer code. This strategy was adopted as in turbomachinery flows (for example) the viscous dominated regions can cover a substantial portion of the flow passage and we use a 'coupling' procedure to integrate the use of the inner and outer flow solutions. The overall concept is shown in *Figure 1*.

The current PNS approach was chosen as it is readily extendible to 3-D. Unlike interacting boundary layer approaches, the PNS equations allow the interactions between the viscous and inviscid portions of the flowfield to be automatically taken into account. The PNS approach is free from any problems patching the boundary-layer and inviscid flow solutions and a constant pressure need not be imposed through the viscous layer as the transverse momentum equation is retained.

GOVERNING EQUATIONS AND SOLUTION METHOD FOR THE INNER PNS CODE

The PNS equations are obtained from full N–S equations[12] by eliminating the time derivative and by neglecting viscous derivatives in the streamwise direction in the momentum and energy equations. The pressure field is assumed to be given and the mass continuity equation now assumes the role of a 'constraint'.

To simplify the treatment of arbitrary geometries and to enhance numerical accuracy and efficiency, a generalized independent variable transformation is employed to map the physical $(x–y)$ plane onto a uniformly-spaced computational $(\xi–\eta)$ plane with constant mesh spacing $\Delta\xi$ and $\Delta\eta$. We assume here that ξ is aligned with the principal flow direction. Considerable

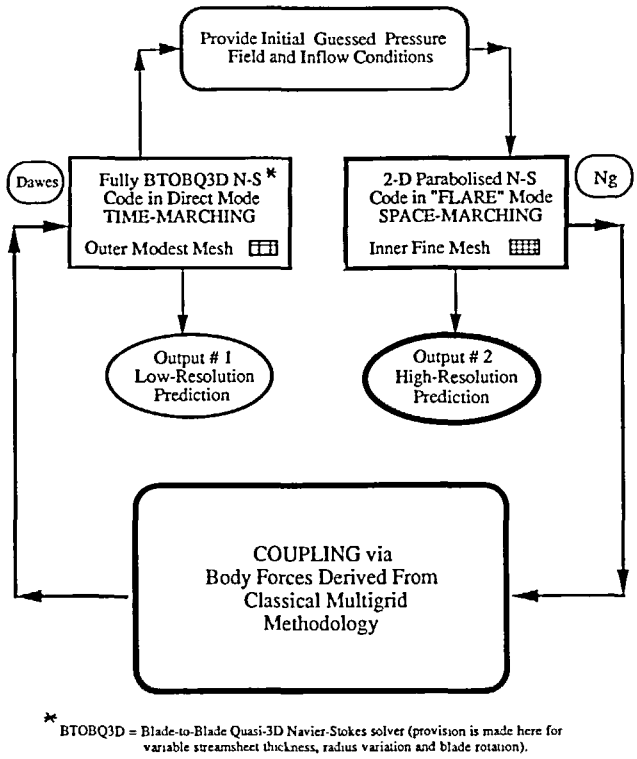

Figure 1 Skeleton flow chart for the coupled inner/outer codes

simplification of the transformed PNS equations were obtained by combining terms carefully and assuming the coordinates ($\xi_x, \eta_y, \eta_x, \xi_y$ etc.) vary slowly compared to the velocity components themselves when calculating the stress tensor and by defining the contravariant velocity components ($\hat{u}, \hat{v}$) along the ξ and η coordinates as variables.

It is desirable to use momentum components aligned with the mesh, so that the streamwise momentum is easily uncoupled from the cross-stream components. Hence, momentum equations and energy equation are written in contravariant form as:

$$C\left|\rho\frac{\hat{u}}{J}\right|\partial_\xi H + \rho\frac{\hat{v}}{J}\partial_\eta H = \partial_\eta \tilde{S} + \tilde{K} \tag{1}$$

$$\frac{\partial}{\partial\xi}\left\{\frac{\rho\hat{u}\left(C_pT + \dfrac{u^2+v^2}{2}\right)}{J}\right\} + \frac{\partial}{\partial\eta}\left\{\frac{\rho\hat{v}\left(C_pT + \dfrac{u^2+v^2}{2}\right)}{J}\right\}$$

$$= \frac{\partial}{\partial\eta}\left\{\frac{(n_x^2+\eta_y^2)\left[\dfrac{\mu}{2}(u^2+v^2)_\eta + kT_\eta\right] + \dfrac{\mu}{3}(\eta_x u + \eta_y v)(\eta_x u_\eta + \eta_y v_\eta)}{J}\right\} \tag{2}$$

with

$$H = \begin{pmatrix}\hat{u}\\ \hat{v}\end{pmatrix}; \qquad \tilde{S} = \frac{1}{J}\begin{pmatrix}\eta_x\tau'_{xx} + \eta_y\tau'_{xy}\\ \eta_x\tau'_{xy} + \eta_y\tau'_{yy}\end{pmatrix}$$

$$\tilde{K} = \frac{1}{J}\begin{pmatrix} \rho G_{\xi p} - g^{\xi\xi}\hat{p}_\xi - g^{\xi\eta}p_\eta \\ \rho G_{\eta p} - g^{\eta\xi}\hat{p}_\xi - g^{\eta\eta}p_\eta \end{pmatrix}$$

$$J = \text{Jacobian} = \frac{\partial(\xi,\eta)}{\partial(x,y)} = \xi_x\eta_y - \eta_x\xi_y = \frac{1}{x_\xi y_\eta - x_\eta y_\xi}$$

$C\left|\rho\frac{\hat{u}}{J}\right|$: FLARE approximation[11] in conjunction with the absolute value of $\rho\hat{u}$; $C = 1.0$ for $\rho\hat{u} > 0$ and $0 \leqslant C \leqslant 0.1$ for $\rho\hat{u} \leqslant 0$.

where

$$\tau'_{xx} = \tfrac{2}{3}\mu(2\eta_x u_\eta - \eta_y v_\eta)$$

$$\tau'_{yy} = \tfrac{2}{3}\mu(2\eta_y v_\eta - \eta_x u_\eta)$$

$$\tau'_{xy} = \mu(\eta_y u_\eta - \eta_x v_\eta)$$

$$\left.\begin{aligned} g^{\xi\xi} &= \xi_X^2 + \xi_Y^2 \\ g^{\eta\eta} &= \eta_X^2 + \eta_Y^2 \\ g^{\xi\eta} &= g^{\eta\xi} = \xi_x\eta_x + \xi_y\eta_y \end{aligned}\right\}\text{are the elements of the contravariant metric tensor}$$

$$G_{\xi p} = \hat{u}(u\xi_{x\xi} + v\xi_{y\xi}) + \hat{v}(u\xi_{x\eta} + v\xi_{y\eta})$$

$$G_{\eta p} = \hat{u}(u\eta_{x\xi} + v\eta_{y\xi}) + \hat{v}(u\eta_{x\eta} + v\eta_{y\eta})$$

$$\left.\begin{aligned} \hat{u} &= \xi_x u + \xi_y v \\ \hat{v} &= \eta_x u + \eta_y v \end{aligned}\right\}\text{they are in directions normal to constant } (\xi,\eta) \text{ surfaces, respectively}$$

k = coefficient of thermal conductivity

C_p = specific heat at constant pressure

The PNS equations are solved using a fully implicit finite-difference scheme with 'lagged' linearized coefficients. The scheme is first-order-accurate in the streamwise direction and second-order-accurate in the transverse direction and it is based on the single sweep forward marching procedure of Briley[2]. Second-order accuracy for the transverse directions is rigorously maintained if the cell Reynolds number is less than an input threshold value (≈ 5 say). The difference equations are solved at each computational plane, marching in the predominant flow direction. All variations, except the pressure, are stored in 1-D arrays. The pressure field is stored two-dimensionally, and is first assigned an initial guessed value from the outer code. It is then corrected iteratively at each station via a pressure correction methodology to remove errors in continuity and momentum. The details of the overall algorithm used to advance the solution a single streamwise step are contained in References 8 and 9.

Assumptions of perfect gas together with the energy equation are used to close the system of equations. A Baldwin–Lomax mixing length turbulence model (BLM) is used but will not be described here as a complete description is given in Baldwin and Lomax[1].

The overall solution procedure requires significantly less computational effort than the outer code algorithm. The present approach is effective even with the extremely fine local mesh resolution which is essential to solve near-wall sublayer regions in turbulent flow calculations.

BOUNDARY CONDITIONS

Boundary conditions are one of the most important aspects in treating internal flow. For the present PNS scheme, the equations are parabolic in the ξ-direction and elliptic in the η-direction.

The initial conditions to start the marching procedure are obtained from the outer N–S code. The coarse solution is then linearly interpolated to obtain the starting solution at the initial data plane for the inner PNS solver. Also, the initial distribution of pressure field for the inner PNS code is established by bilinear interpolation from the outer code. For the present scheme, the boundary conditions at the wall (other than the jet exit plane) consist of (1) the no-slip and impermeability conditions for U_i velocity component; (2) zero pressure derivative (Neumann condition) in the η-direction.

Before the coupling routine is first used, the boundary conditions employed in the outer N–S code are consistent with the inner PNS code. However, for a coupled calculation, the inner code is solving for the details of the flow ('master') whilst the role of the outer solver is to propagate information (mainly 'blockage' elliptic-effects) concerning the fine mesh solution to the flow field at large. Fine mesh accuracy is obtained by causing the coarse grid solution to be driven by the fine mesh residues. Thus, the issue of the consistency for the boundary conditions does not arise.

OUTER N–S SOLVER

The outer coarse N–S (or Euler) solver used in the present work has been described elsewhere in various applications[3,4] and is used here to provide an initial guess of pressure field for inner fine PNS code. However, it is noteworthy to mention that for current application, the criteria for the first grid point away from duct wall surface is chosen to be $\Delta y_1 \approx 10 \times$ duct length $\times \sqrt{Re_c}$ where Re_c is the Reynolds number based on duct length, this gives Y^+ (for turbulent case $= \sqrt{\{\rho_w \tau_w\}} \cdot y/\mu_w) \approx 0(35)$, and therefore requires a slip velocity when employing wall function modelling.

THE PNS/NS COUPLING PROCEDURES

In this section, we will outline the coupling between the outer time-marching scheme and the inner space-marching code. For brevity, only a summary of the coupling procedure is presented, the actual details can be found in Reference 9.

The guiding principle of the current coupling implementation is that the inner code is driven by the pressure field of the outer code whereas the latter is driven by the former by averaging the fine solution onto the coarse mesh in an analogous way to classical multigrid methods, so producing effective stresses for the outer code. On the coarse mesh, effective coupling stress terms are added to the R.H.S. of the N–S equations interpreted as 'source-terms' represented by the 'collected' space-averaged fine mesh 'perturbation fluxes' that surround the coarse node. In the current context, the collected fine mesh fluxes can be thought of as containing generalized 'displacement thickness' type information. The coarse grid solution and fine grid prediction proceed in parallel with the rate of convergence being determined mainly by the coarse mesh and the accuracy being decided by the fine mesh.

For a coupled calculation, the effective stress terms are computed only at specified coupling time-steps (e.g. 50 or 100, no adaptive criterion is being implemented) and then remain fixed until the next coupling step is initiated. Additional storage is required for the effective stress term; but, because of the relatively reduced number of grid points in the outer code, all arrays needed by the original algorithm are reduced in size. The net effect is a substantial reduction in storage requirements. In a classical multigrid strategy, the same type of solver is used on all the meshes[5,10]; however, this is nevertheless very expansive on fine mesh. The novelty here is to use a cheap PNS solution procedure on the finest mesh. A multigrid 'coupling' recipe is used to link the inner and outer codes and the forcing function ensures fine mesh accuracy by causing

the coarse grid solution to be driven by the fine mesh residues as follows:

(1) obtain an inner fine grid solution with PNS code with $\Delta U^{\text{fine}} = 0 = (\text{R.H.S.})^{\text{fine}}$;

(2) for each inner fine cell, calculate $(\sum \text{fluxes})^{\text{fine}}$ and sum over all the fine cells within each coarse cell to form $\sum_{\text{fine cells}}^{\text{coarse mesh}} \left(\sum \text{fluxes}\right)^{\text{fine}}$;

(3) space-average $\left(\text{e.g. } \bar{u} = \frac{1}{\text{vol}} \int u \, \text{d(vol)} \text{ etc.}\right)$ fine mesh variables projected onto the outer coarse grid and compute $\left(\sum \text{fluxes (average-variables)}\right)^{\text{coarse}}$;

(4) calculate the 'effective' coupling stresses for each coarse node in the form of 'source term'$^{\text{coarse}} = \sum_{\text{fine cells}}^{\text{coarse mesh}} \left(\sum \text{fluxes}\right)^{\text{fine}} - \sum_{\text{coarse cells}} \text{flux (average-variables)}$;

(5) solve NS elliptic equations on coarse grid code for

$$\Delta U^{\text{coarse}} = (\text{R.H.S.})^{\text{coarse}} + \text{'source term'}$$

$$\left|\leftarrow \text{original outer code} \rightarrow\right| \quad \left|\leftarrow \text{driven to provide} \rightarrow \text{fine mesh accuracy}\right|$$

Define a suitable collection operator $(\mathbf{I})_{\text{fine}}^{\text{coarse}}$, and a forcing function as:

$$\text{'source-term'} = \mathbf{I}_{\text{fine}}^{\text{coarse}} (\text{R.H.S.})^{\text{fine}} - (\text{R.H.S.})^{\text{coarse}}$$

$$= \sum_{\text{fine cells}}^{\text{coarse mesh}} \left(\sum \text{fluxes}^{\text{fine}}\right) - \sum_{\text{coarse cells}} \text{flux (average-variables)}$$

The coupling procedures have been applied to the following five 'known' boundary-layer profiles[9], namely: (a) parallel channel and Couette flow, (b) self similar laminar boundary flow for the exact Blasius solution, (c) a turbulent boundary layer flow from the Stanford proceedings data (1968) and (d) flow through a compressor cascade and a turbine cascade where generally favourable results are obtained, particularly for the compressor cascade. The most noteworthy feature of these comparisons, is that when the inner mesh is refined further, the effect of the space-averaged 'coupling-stresses' is increasingly more significant as expected[8] and the agreement with the data is good. However, when the inner sub-grid is further refined, the effect of these 'coupling-stress source terms' tends to converge to a certain level gradually. Comparisons are also given with traditional boundary layer predictions to illustrate the significance of the coupling effects modelled by the present method. For the extreme case (a), even for only a single node in the outer code, the inner solver will still produce an appropriate source term which is correctly related to the known wall shear stress law[9].

CONVERGENCE CRITERIA AND RELATIVE CPU TIME FOR THE COMPOSITE SOLUTION

At the end of each time step of the coupling procedure, a check is made as to whether the flow problem has converged. Convergence of the coupled flow field is defined to be achieved when the maximum change in axial velocities between the inner and the outer codes at any grid point in successive time steps is within a tolerance of 0.05%. That is, we use $(\|U_{\text{outer}} - \bar{U}_{\text{inner}}\|/U_{\text{ref}}) \Rightarrow 0$ as a measure of the 'inner/outer' composite convergence criteria. In this way, both the $\bar{U}_{\text{inner}}$ and U_{outer} will satisfy the global and local mass constraints and force the compatibility of the

pressure fields. Typical coupled calculations using a 98 streamwise by 45 tangential computational grid take 400 outer iterations. All of the above-mentioned computations are performed on an Alliant fx-80 mini-computer of Whittle Laboratory, Cambridge. The relative CPU time for the coupled code is approximately 4 to 5 times less than would be required using a full outer N–S solver alone with the same number of mesh points. That is, the present approach allows an order-of-magnitude improvement in resolution of the viscous region and requires considerably less computation time.

DESCRIPTION OF THE PROBLEM

The aim of the work to be described in the following section is to provide an example of an application for the coupled code in predicting the film cooling effectiveness distribution downstream of an angled slot. The film system nomenclature is shown in *Figure 2*. The geometry of the film-cooled surfaces on turbine vane sets is modelled using a plane heat-transfer surface with a unit width in a constant cross-sectional area flow passage. The relative sizes of the duct cross section and injection slots were chosen to correspond to the experimental configuration of Metzger *et al.*[13].

COMPUTATIONAL METHOD

Coolant ejection from slots in the plate surface may be included in the present PNS solver, space-marching calculation by the addition of the jet exit boundary conditions to the momentum, continuity and energy equations. The energy equation is required as the wall temperature downstream of the slot is not a uniform distribution. Mixing of secondary and mainstream fluids may then occur, and the stagnation pressure loss across the cooling film should be automatically calculated.

Assumptions and mesh used for the calculation approach

(a) The PNS calculation begins from an upstream plane which is located well before the injection slot. By doing this, all the errors that might have been induced near to the leading edge singularity point of the test surface are mitigated by the parabolic characteristic of the equation.

(b) The slot exit velocity profile is nearly uniform. This assumption is very crude as the conditions across the jet exit are highly non-uniform. This strongly suggests that in modelling

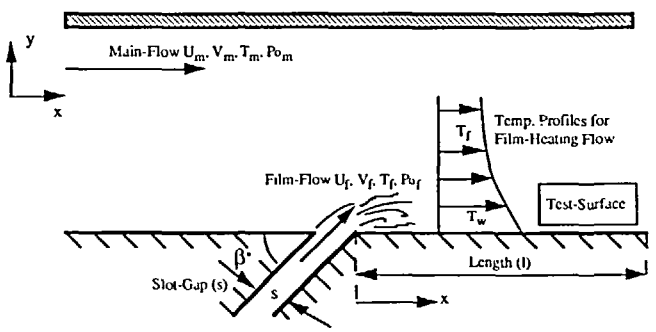

Figure 2 The flow situation under consideration

the ejection with conventional structured codes such as that used in this work, it may not be adequate to specify the ejection simply in terms of a uniform normal flux superimposed on the regular surface boundary condition.

(c) The fluids involved are air, and the temperature differences are sufficiently small for the thermodynamic and transport properties involved to be considered nearly constant. This assumption is consistent with a linear formulation of the energy problem. The variations of stagnation temperatures and mass flow rates, G^* ($= G_f/G_m$ where G_f and G_m are the mass flow rates per unit area of the film and mainstream respectively), are assumed to be relatively small and the mainstream and coolant specific heats are assumed equal ($\gamma_m = \gamma_f$). This implies that film cooling ($t_m > t_f$) and film heating ($t_m < t_f$) are similar problems governed by the same differential equations and boundary conditions for film effectiveness and heat-transfer coefficient. As film heating is more frequently and more conveniently investigated experimentally, we will consider the heating of main flow ($t_m < t_f$).

A 98 × 45 computational H-mesh was used for the coarse outer N–S code. The inner PNS solver used a mesh of 2× refinement with respect to this basic background mesh. In order to resolve the sub-layer, the distance of the first grid point from the test surface was taken to be the order of two viscous units, Y^+ ($= \sqrt{\{\rho_w \tau_w\}} \cdot y/\mu_w$) $\approx 0(2)$. This gave the typical number of grid points within the boundary layer of 20 and no wall function modelling is required. The PNS solver needed only 1.597×10^{-4} sec of CPU time per step per grid point.

Boundary conditions at the jet exit plane

The velocity emerging from the injection slot was treated as uniform across the slot-gap, with the streamwise and normal components obtained as:

$$\text{Temperature } T_{s1} = T_{\text{film}} \quad (\text{at jet exit } y = 0)$$

$$\text{Velocities } U_e = U_{\text{film}} \cdot \cos\beta \quad \text{and} \quad V_e = U_{\text{film}} \cdot \sin\beta$$

It is known that the assumption of a uniform stagnation pressure in the jet discharge plane offered, in some cases, a boundary condition that would more closely approximate the actual condition than that of a uniform inlet velocity, particularly at higher injection rate. The problem of uncertainties in the flow conditions at exit from the injection slot can best be dealt with by extending the numerical computations some distance into the injection slot itself; this, however, could not be attempted here.

BASIC CONSIDERATIONS AND THE GOVERNING PARAMETERS

With the nomenclature and coordinate system as in *Figure 2*, it was expected that the local heat-transfer rates downstream of the injection location would be influenced by the properties of the mainstream fluid and its velocity, U_m, the properties and velocity, U_f, of the secondary fluid, the temperatures t_m, t_f and t_w of the mainstream, the secondary stream and the wall; the injection geometry (S and β); and the downstream distance x. In the present study, average surface heat-transfer rates were calculated over a finite x distance, l, downstream of injection. These rates were compared to the heat-transfer rate predicted with the same surface and mainstream conditions in the absence of any injection slots. The ratio of average surface heat transfer with blowing to that without, ϕ, is presented non-dimensionally as:

$$\phi = \phi(\Theta^*, G^*, L/S, \text{geometry})$$

where

$$G^* = \frac{G_f}{G_m} \quad \& \quad \Theta^* = \frac{t_f - t_m}{t_w - t_m}$$

G_f and G_m are the mass flow rates per unit of the film and mainstream, respectively, and S is the actual width of a two-dimensional injection slot (or for the case of the hole injection, the width of an equivalent slot of equal discharge area). Note that in this work, the mainstream Reynolds number ($G_m l/\mu$) was varied by changing both the mainstream velocity and surface length l, but an extensive independent variation and study of the effect of Prandtl number were not made. A Prandtl number of 0.92 was used.

PREDICTED FILM COOLING EFFECTIVENESS VS. EXPERIMENTAL CORRELATED DATA

Although the numerical calculations were carried out in physical units, the results have been made dimensionless in accordance with the nomenclature of Metzger[13] to facilitate comparison. Representative calculations of film cooling performance for three injection angles, $\beta = 20°$, 40° and 60° were performed and the results are compared with Metzger *et al.*'s experimentally correlated results. The effect of the injected film is illustrated in terms of the ordinate ϕ, defined as: $\phi = (h)_{\text{with film injection}}/(h)_{\text{without film injection}}$, *versus* the non-dimensional group of $\Theta^* G^{*0.6}(S/L)^{0.5}$. Plots of flow vectors and static pressure contours are also presented.

Effect of slot angle β variation

Figure 3 summarizes the effect of varying the slot angles β. A low angle results in a reduced coolant normal momentum flux with less coolant penetration into the boundary layer (i.e. the rate of vertical spread is less) and hence improved cooling effectiveness. The larger the injection angle ($\beta = 60°$ say), the smaller the film cooling effectiveness due to the fact that the coolant stream has sufficient energy to penetrate deeply into the main gas stream which induces greater mixing of the coolant with the mainstream at the point of injection. These phenomena are consistent with the contour plots for the Mach number and stagnation temperature and the velocity vector diagrams[9]. *Figure 4* also shows that when β is increased from 20° to 60°, the average intersection on both the ordinate (ϕ) and abscissa ($\Theta^* G^{*0.6}(S/L)^{0.5}$) is increased. In practice, the angle between the direction of the slot and the surface is kept as small as possible to minimize the penetration of the coolant into the main gas flow and the related reduction in cooling and aerodynamic performance of the component.

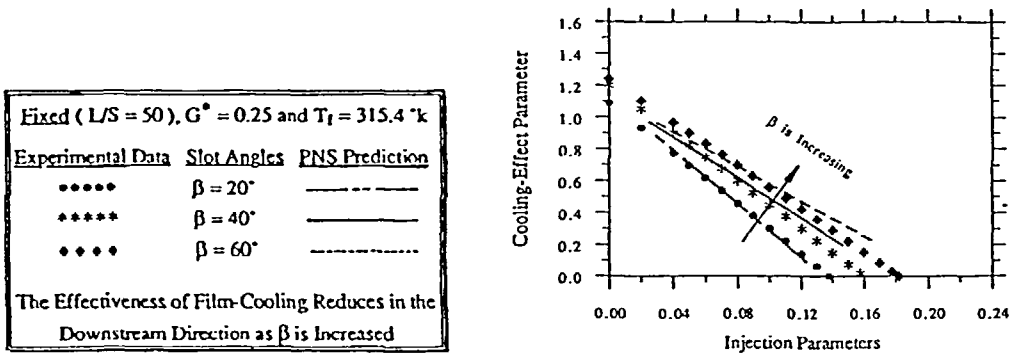

Figure 3 The effect of slot-angles β *vs* variation

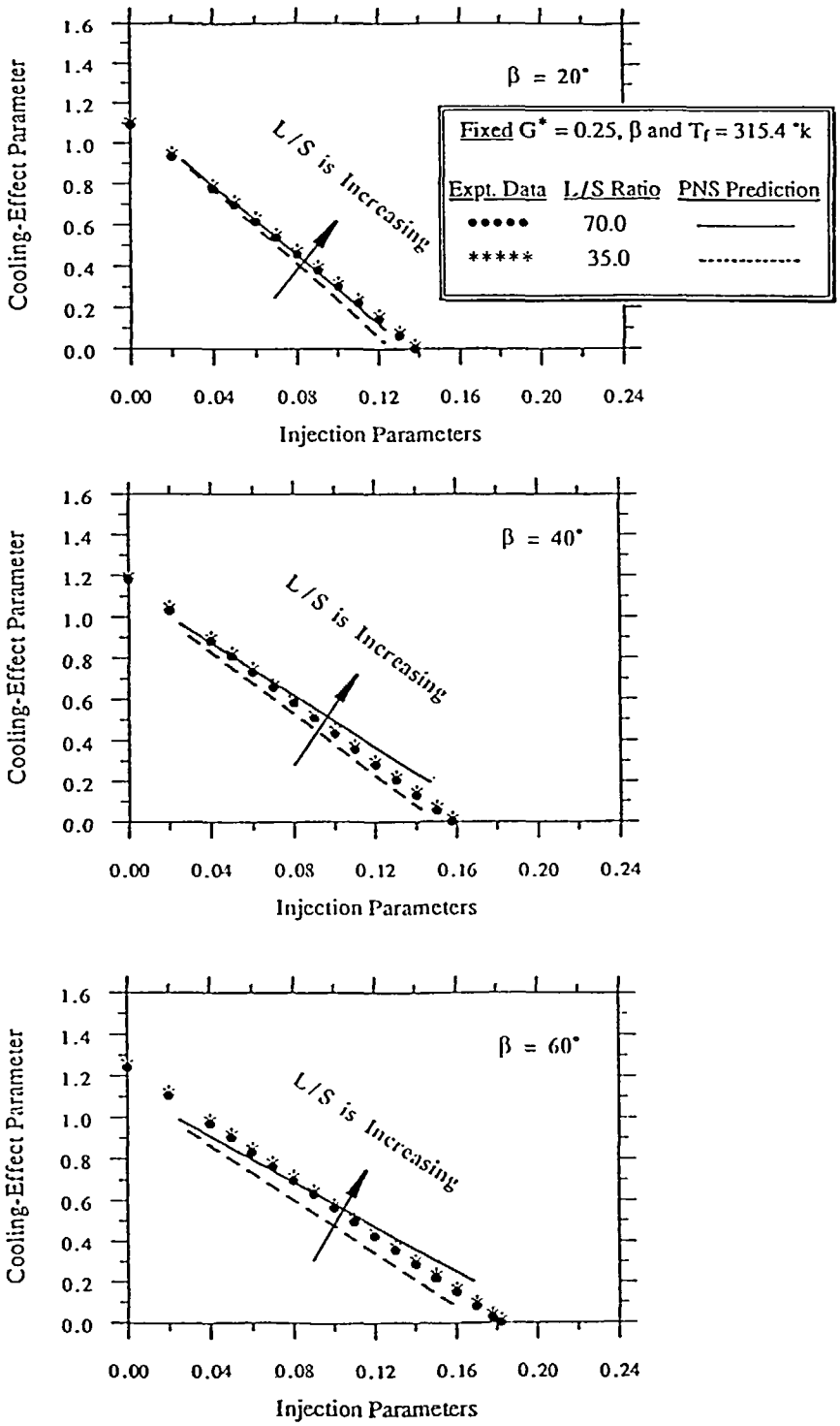

Figure 4 The effect of changing the test surface geometry (L/S) ratio

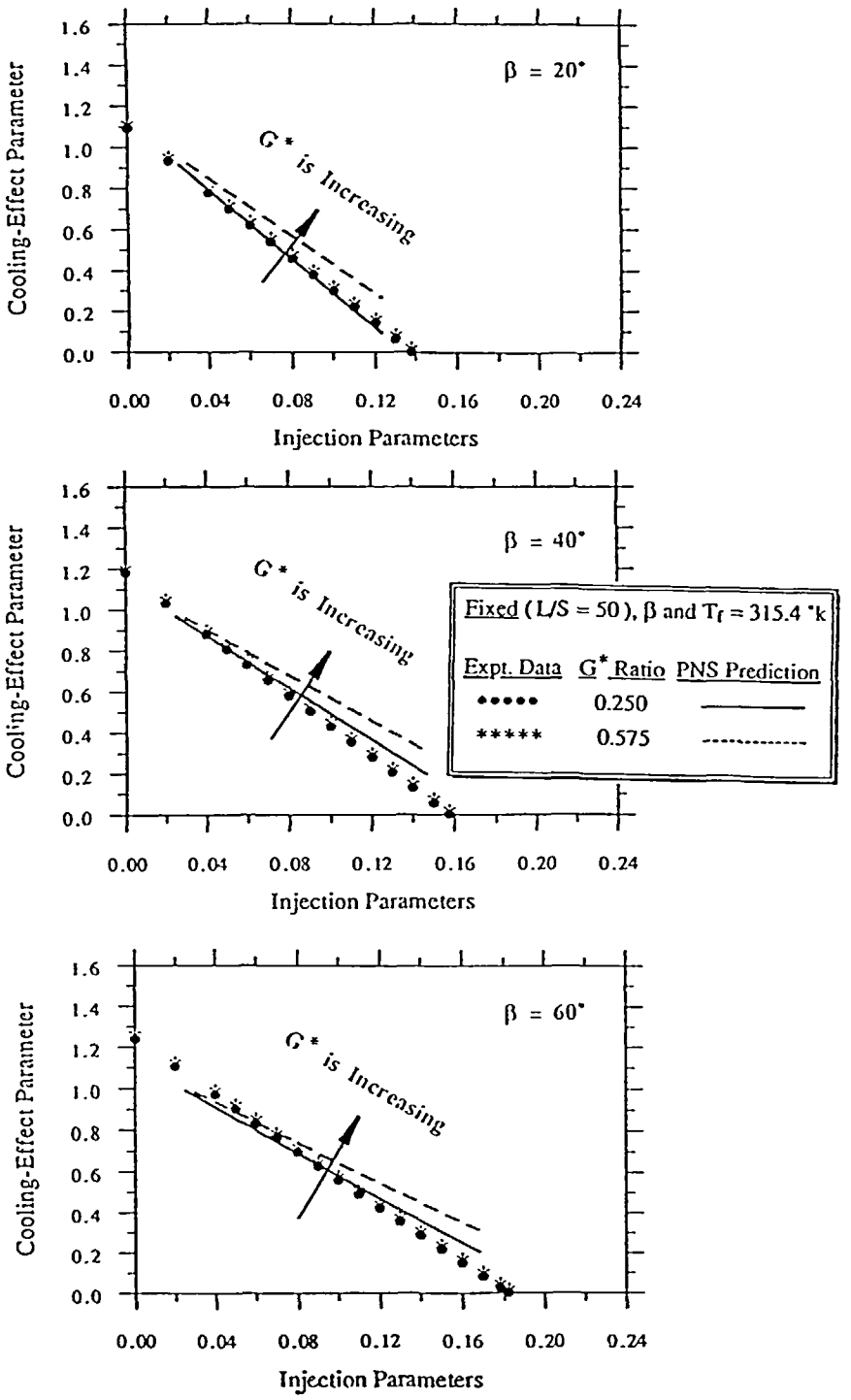

Figure 5 The effect of varying G^* mass velocity ratio $= \dfrac{(\rho u)_f}{(\rho u)_m}$

Effect of changing the slot-gap/surface-length (S/L) ratio

Figure 4 presents results obtained by varying the (S/L) ratio for a respective constant slot angle β. As expected, the reduction in heat transfer (ϕ) for $L/S = 70$ (the largest value in this investigation) is somewhat less than corresponding values at smaller L/S ($= 35$ say) for all values of G^* and β. This reduction in film performance reflects increased mixing between the film and main flows with increasing L/S. In other words, when the values of (L/S) is sufficiently low, the entire surface is effectively blanketed by the film air, and the heat transfer rate approaches zero as $t_w = t_f$ or as $\Theta^* \left(= \dfrac{t_f - t_m}{t_w - t_m} \right)$ approaches unity.

Effect of mass velocity ratio $G^* = (\rho u)_f/(\rho u)_m$

Figure 5 demonstrates the film cooling effectiveness (ϕ) as a function of the mass velocity ratio $(G^* = (\rho u)_f/(\rho u)_m)$ with $(\Theta^* G^{*0.6}(S/L)^{0.5})$. One observes that the film cooling effectiveness, ϕ, for the single slot increases at first (from 0.25 to 0.5) with increasing G^* and then decreases again for G^* values beyond about 0.5. At high values of G^*, the coolant penetrates to the mainstream and an insufficient film cooling layer is generated on the surface downstream of the slot. It is noteworthy that the predictions are exhibiting a well-known phenomenon usually termed 'lift-off' whereby the effectiveness reaches a maximum with an increasing injection rate and then subsequently decreases. It is also worthy of note that there are indications in the existing literature[6] that, in reality, the penetration of a jet into the surrounding fluid generally depends on the momentum flux rate $(I = (\rho u^2)_f/(\rho u^2)_m)$ rather than the mass flux rate $(G^* = (\rho u_f)/(\rho u)_m)$.

CONCLUDING REMARKS

The present paper has described a methodology for coupling relatively coarse mesh N–S solutions to PNS solutions performed on a much finer sub-mesh. The fine mesh provides enhanced accuracy and is coupled to the outer code in an analogous way to a multigrid method so that the outer code provides fast, global convergence. The principal conclusions which can be drawn from the present work are set out below. It should be remembered that these remarks apply only to a two-dimensional, constant property flow.

(a) The effect of an increase in the injection angle is to decrease the effectiveness. The effectiveness of film cooling obtained from an angled slot is, therefore, expected to be greater than that obtained from tangential (90°) injection.

(b) The solution of the PNS with the energy equation is dependent on the initial velocity and temperature profiles and boundary conditions at the coolant exit. Experimental data could also be used for initial conditions instead of using: either (a) the uniform stagnation temperature T_0 and stagnation pressure P_0 assumptions and by extending the computational grid some distance into the injection slot itself; or (b) imposing a linear increase in the jet exit velocity from just upstream to just downstream of the slot edges.

(c) In the vicinity of the discharge slot at high blowing rate ($G^* = 1.0$), the upstream pressure effects will introduce an element of ellipticity which precludes the use of a purely forward-marching procedure and necessitates the coupling of N–S and PNS solver in order to account for the elliptic effect. For example, with $G^* = 1.0$ and $\beta = 20°$ as shown in *Figures 6* and *7*, there is only a small displacement of the boundary layer upstream of the slot but a substantial displacement of the profile behind the slot with a large wake in the boundary layer. However, for $\beta \geqslant 40°$, the mainstream fluid is deflected upward in the upstream of the jet; downstream of the slot, a clockwise-rotating vortex with length of the order of one slot width is clearly visible. This arises from the vorticity introduced by the injection and is predicted using the current coupling

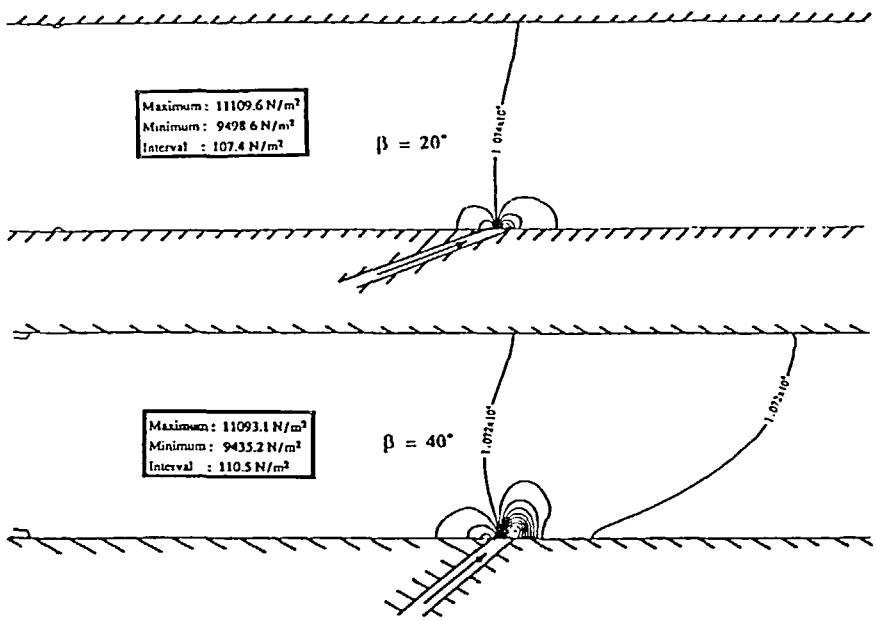

Figure 6 Predicted static pressure contours for $G^* = 1.0$

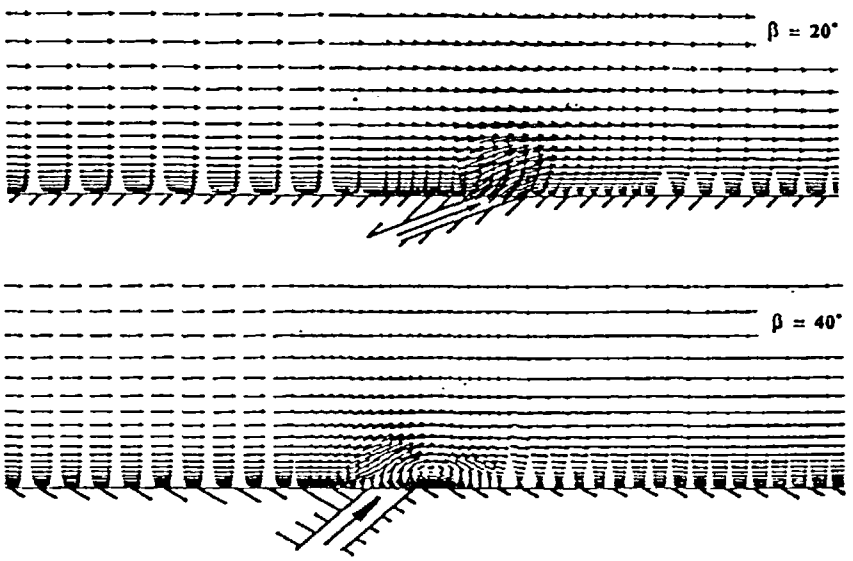

Figure 7 Predicted absolute velocity vectors for $G^* = 1.0$

methodology. The present uncoupled purely PNS code is unable to cope with such an extensive separation region immediately downstream of the slot.

(d) The overall agreement with the present calculations is generally good. The discrepancies far downstream of the slot (especially when slot-angle β or blowing rate G^* is increased) might

be attributable to three causes. First, the initial values used for the numerical computations do not precisely specify the experimental conditions at that point, notably the jet exit boundary layer conditions and the density ratio. Secondly, the predictions assume that the detail flow situation is governed by the PNS equations. Finally, the turbulence model used may be inadequate for this flow environment, especially with the presence of several local velocity maxima. It would seem more appropriate to use a more physically-based turbulence model, instead of the simple Baldwin–Lomax zero equation model and to include all the various secondary production terms.

(e) Obviously, the blade film cooling effectiveness may be measured experimentally. Such a course of action, however, is very expensive, and too time consuming to be of use in the iterative design and optimization process. An accurate computer program capable of giving predictions of the surface film cooling effects on gas turbine blades would be of great assistance to engine designers and should also help to reduce the amount and hence cost of development testing required in an engine design. Therefore, further work on accurate 3-D numerical calculations for film cooling injected at an angle to the mainstream with high-speed flow and with large density differences may even prove very worthwhile.

ACKNOWLEDGEMENTS

The author is indebted to Dr. W. N. Dawes of Cambridge University for the supply of his 2-D Navier–Stokes 'outer' code.

REFERENCES

1 Baldwin, B. S. and Lomax, H. Thin layer approximation and algebraic model for separated turbulent flows, *AIAA Paper No 78-257* (1978)
2 Briley, W. R. Numerical method for predicting 3-D steady viscous flows in ducts, *J. Comput. Phys.*, **14**, 8–28 (1974)
3 Dawes, W. N. Computation of off-design flows in a transonic compressor rotor, *ASME J. Eng. Gas Turb. Power, Paper No 85-GT-1* (Dec. 1985)
4 Dawes, W. N. Application of full N–S solvers to turbomachinery flow problems, *VKI Lecture Series 1986-02*, Numerical Techniques for Viscous Flow Calculations in Turbomachinery Bladings (Jan. 1986)
5 Dawes, W. N. The application of multigrid to N–S simulation of 3-D flow in axial and radial turbomachinery, *J. Num. Meth. Fluids*, **8**, 1217–1227 (1988)
6 Eckert, E. R. G. Film cooling with injection through holes, *AGARD Conf. Proc. High Temp. Turb., AGARD CP-73-71* (1971)
7 Goldstein, R. J. Film cooling, *Advances in Heat Transfer*, Vol. 7, Academic Press, New York (1971)
8 Ng, E. Y.-K. and Dawes, W. N. A novel approach to high resolution compressible cascade flow analysis using the Navier–Stokes equations, *ASME Paper No 92-GT-419* (June 1992)
9 Ng, E. Y.-K. A high-resolution coupled parabolic/elliptic Navier–Stokes solver for turbomachinery flows, *PhD Thesis*, University of Cambridge (June 1992)
10 Ni, R. H. A multi-grid scheme for the Euler equations, *AIAA Paper 81-1025* (1981)
11 Reyhner, T. A. and Flügge-Lotz, I. The interaction of a shock wave with a laminar boundary layer, *Int. J. Non-Linear Mech.*, **3**, 172–199 (1968)
12 Roache, P. J. *Computational Fluid Dynamics*, Hermosa Publisher, Albuquerque, NM (1982)
13 Metzger, D. E., Carper, H. J. and Swank, L. R. Heat transfer with film cooling near nontangential injection slots, *ASME J. Eng. Power*, **90A**, 157–163 (1968)